ACSNANO

www.acsnano.org

ARTICLE

Regulating the Electrical Double Layer with Supramolecular Cyclodextrin Anions for Dendrite-Free Zinc Electrodeposition

Lulu Wang,[⊥] Chengzhen Shen,[⊥] Chaoran Huang, Jitao Chen,* and Junrong Zheng*

Cite This: *ACS Nano* 2023, 17, 24619–24631

Read Online

ACCESS | Metrics & More | Article Recommendations | Supporting Information

ABSTRACT: The interfacial stability of a Zn battery is dependent on the electrical double layer (EDL) that forms at the interface between the electrolyte and the Zn metal anode. A fundamental understanding of the regulation of the EDL structure and stability on the Zn surface is highly desirable for practical applications of aqueous batteries. Herein, the interfacial chemistry of the EDL is regulated by the adsorption of supramolecular cyclodextrin anions in the inner Helmholtz plane (IHP). The nucleation overpotential and the charge transfer activation energy for Zn^{2+} to go through the OHP (Ea_1) and IHP (Ea_2) are increased, leading to slower Zn^{2+} transfer kinetics. The electric field distribution and Zn^{2+} flux in the proximity of the Zn metal surface are homogenized, thus suppressing the growth of dendrites. The mechanism is supported with theoretical and experimental analyses. Consequently, a Zn||Zn symmetric cell achieves an ultrahigh cumulative capacity of 10000 and 4250 mAh cm^{-2} at a respective current density of 10 and 50 mA cm^{-2}, and an average Coulombic efficiency of 99.5% over 1000 cycles under harsh conditions (at a high current density of 10 mA cm^{-2} with a high capacity of 10 mAh cm^{-2}). This work provides insight into the introduction of supramolecular anions to regulate the electrical double layer EDL structure and improve the interfacial stability.

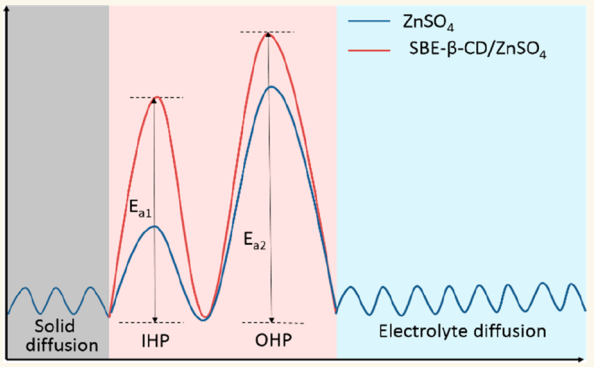

KEYWORDS: *EDL regulation, interfacial stability, supramolecular cyclodextrin anions, aqueous Zn battery, Zn dendrites suppression*

INTRODUCTION

High cost and safety concerns impede the large-scale deployment of successfully commercialized Li-ion batteries (LIBs). Rechargeable aqueous Zn-ion batteries (ZIBs) are promising alternatives in grid-scale energy storage applications due to their high theoretical capacity (820 mAh g^{-1})[1] and the high abundance of Zn anode,[1,2] the intrinsic safety[3] and facile manufacture.[9] However, the unavoidable defects on the Zn electrode surface during manufacturing can act as dendrite nucleation seeds and trigger the growth of Zn dendrites that significantly shorten the lifespans of batteries.[4] At low current densities and capacities (e.g., under the Sand's capacity), mossy Zn grows from the roots.[5−7] At high current densities and capacities (e.g., above the Sand's capacity), wispy Zn dendrites rapidly grow on the tips. Zn-ion flux is more concentrated on the tips of the rough Zn surface due to the enhanced local electric field, leading to self-amplification and eventually evolution into Zn dendrites. According to Sand's model, how the electric field is distributed in the vicinity of the Zn surface is the leading control factor for the formation of dendrites. The intensity of the electric field at protrusions with higher curvature, especially at the sharp tips, is much higher than that at other areas.

Recently, various strategies have been developed to enhance the Zn electrode reversibility including, electrolyte optimization,[8−11] anode structure design, constructing solid/electrolyte interphases,[12−14] and adopting Zn alloys,[15] etc. Among them, electrolyte optimization is the most practically expedient strategy since it does not involve complicated preparation processes, introduce too much extra weight, or increase manufacture cost. To date, many types of additives have been investigated to stabilize the Zn anode. For instances, Wang et al.[16] introduced dimethyl sulfoxide (DMSO) into 2 M $ZnSO_4$ to replace H_2O in the solvation sheath of Zn^{2+}, which

Received: April 10, 2023
Revised: November 19, 2023
Accepted: November 28, 2023
Published: December 5, 2023

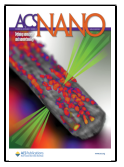

https://doi.org/10.1021/acsnano.3c03220
ACS Nano 2023, 17, 24619−24631

suppressed the electrolysis of solvated H_2O, thus enabling the Zn||Zn cell stably cycle for 1000 h at 0.5 mA cm^{-2} with 0.5 mAh cm^{-2}. Zhu et al.[17] reported that a cationic surfactant-type electrolyte additive tetrabutylammonium sulfate (TBA_2SO_4) can induce uniform Zn deposition via zincophobic repulsion mechanism, which extends the lifetime of Zn||Zn cell to 160 h at 5 mA cm^{-2} with 5 mAh cm^{-2}. Despite the improved cyclability of Zn metal anodes with various additives at low current densities and small area capacities, the electrochemical stability of Zn anodes is still far from meeting the demands for practical applications under the condition of high current densities and large capacities (current densities ≥5 mA cm^{-2} and areal capacities ≥5 mAh cm^{-2}). Therefore, it is indispensable to explore additives capable of suppressing dendrite growth and interfacial side reactions at high current densities and large capacities.

Up to now, limited attention has been paid to the role of electrical double layer (EDL) structure in promoting the interfacial stability.[18,19] Although the solid electrolyte interphase (SEI) is very important, the evolution of EDLs at the electrode/electrolyte interface can be critical, as well. The Graham and Bockris−Devanathan−Muller (BDM) model of EDL consists of an inner Helmholtz plane (IHP), an outer Helmholtz plane (OHP) and a diffusion layer.[20] In general, when a metal electrode is brought into contact with the electrolyte, adsorbed ions or molecules are located in the IHP and opposite-charged solvated ions are located in the OHP. The diffuse layer with a net charge has a nonuniform salt concentration. The electric potential in the EDL decreases linearly in the Stern layer and then exponentially in the diffuse layer. The ion transport/charge transfer at the electrode/electrolyte interface in batteries relies on the structure of EDL.[20,21] The EDL structure influences the electric potential distribution within these layers, thereby greatly dictating the electrochemical reaction mechanism and rates. For instance, it has been reported that regulating the adsorption species in the IHP effectively accelerates the thermodynamics and dynamics of Li^+ diffusion from electrolyte to Li-metal surface.[22] Xu et al.[23] found that the working voltage and cycling ability of aqueous Li-ion batteries could be improved by tailoring the IHP interfacial structure. Hence, regulating the EDL structure and its electric field distribution provides a promising pathway to improve the interfacial stability near the anode.

Cyclodextrins (CDs) are a class of cyclic oligosaccharides obtained from renewable enzymatic degradation of starch.[24] They usually possess a chair conformation consisting of six, seven, or eight D-(+)-glucopyranosyl units linked by α-1,4-glycosidic bonds, featuring a hydrophobic internal cavity and a hydrophilic outer surface. Due to the feature, CDs have been widely applied in various industrial applications including pharmacy foods, chromatography, and etc.[25] Recently, the electrically neutral CD molecules including α-CD, β-CD and γ-CD have been added into electrolyte to either boost Zn plating kinetics[26] or improve Zn^{2+} migration behaviors by anion-trap,[27] thus inhibiting Zn dendrite growth and enhancing cycling stability at relatively low current densities and areal capacities. However, the effect is limited at low current densities and capacities because natural CDs are electrically neutral and barely soluble in 2 M $ZnSO_4$ aqueous electrolyte, which can hardly alter the EDL structure at the interface.

Herein, instead of electrically neutral CDs, a supramolecular anionic sulfobutyl ether β-cyclodextrin (SBE-β-CD) with an average substitute degree of 2 ($C_{50}H_{84}O_{41}Na_2S_2$, M = 1451) (Figure S1) is introduced into the IHP to tailor the EDL structure at the anode/electrolyte interface. The anionically charged SBE-β-CD is highly soluble in concentrated $ZnSO_4$ in aqueous electrolytes. It is of low toxicity, and has a lower Zeta potential due to the anionic nature of the substituents.[28,29] These features endow SBE-β-CD with the ability to regulate the EDL structure, which plays a vital role in improving the interfacial stability. Both theoretical and experimental analyses confirm the preferential adsorption of cyclodextrin anion on the Zn (0002) plane over H_2O. On one hand, the entrance of cyclodextrin anions into the inner Helmholtz plane (IHP) increases the thickness of EDL, which increases nucleation overpotential (from 36.8 to 39.9 mV) and the charge transfer activation energy for Zn^{2+} to go through the OHP (Ea_1, from 14.63 kJ mol^{-1} to 34.92 kJ mol^{-1}) and IHP (Ea_2, from 37.16 kJ mol^{-1} to 46.97 kJ mol^{-1}) and thus slows down the Zn^{2+} transfer kinetics. On the other hand, the introduction of cyclodextrin anions into the IHP homogenizes the electric field distribution and Zn^{2+} flux within the EDL, resulting in a dense and even Zn electrodeposition. In addition, the decline in the number of water molecules in IHP due to preferential adsorption of the SBE-β-CD anion compared to water impedes the H_2 evolution. As a result, a Zn||Zn symmetric cell achieves an ultrahigh cumulative capacity of 10000 and 4250 mAh cm^{-2} at respective current density of 10 and 50 mA cm^{-2}, and an average Coulombic efficiency of 99.5% over 1000 cycles under harsh conditions at a high current density of 10 mA cm^{-2} with high capacity of 10 mAh cm^{-2}. The differences between this work and works with neutral additives are analyzed in Supplementary note 1.

RESULTS AND DISCUSSION

Evolution of EDL Structure after Introducing SBE-β-CD Anion. To unravel whether SBE-β-CD can absorb on the surface of Zn foil anode, the surface condition of the Zn anodes after immersion in a 5 mM SBE-β-CD aqueous solution (Figure S1) for 4 h is investigated with comprehensive characterizations. Zn foil was ultrasonicated in deionized water for 30 min and rinsed with deionized water and ethanol for several times after Zn foil was immersed in a 5 mM SBE-β-CD aqueous solution to remove the remaining SBE-β-CD and dried for further characterization. The EDS mapping of the Zn plate (Figure S2) shows that S, O, and C elements distribute uniformly on the surface of Zn, which provides direct proof of the absorption behavior. X-ray photoelectron spectroscopy (XPS) and Fourier transform infrared spectroscopy (FTIR) measurements are carried out to further explore whether the SBE-β-CD is adsorbed on the Zn surface. The FTIR spectrum of the SBE-β-CD/$ZnSO_4$ electrolyte almost overlaps with that of the $ZnSO_4$ electrolyte (Figure S3), suggesting that a few SBE-β-CD additive ions exert little effect on the Zn^{2+} solvation structure. HNMR was used to further investigate the effect of SBE-β-CD on the solvent structure of Zn^{2+}. The water proton (^2H) peak shifts very slightly to high field (from 4.723 (blue) to 4.722 (red) ppm) after 5 mM SBE-β-CD was added to 2 M $ZnSO_4$ electrolyte (Figure S4a), whereas with only 5 mM SBE-β-CD and without $ZnSO_4$ the water proton peak (black) is at a much higher field 4.70. The result clearly indicates that 2 M $ZnSO_4$ but not 5 mM SBE-β-CD can significantly influence water. In other words, 5 mM SBE-β-CD must not alter the solvation structure of Zn^{2+} in a significant way. Because of its high concentration, 2 M $ZnSO_4$ electrolyte can also affect SBE-β-CD. The proton (^1H) peaks of SBE-β-CD shift obviously to

https://doi.org/10.1021/acsnano.3c03220
ACS Nano 2023, 17, 24619−24631

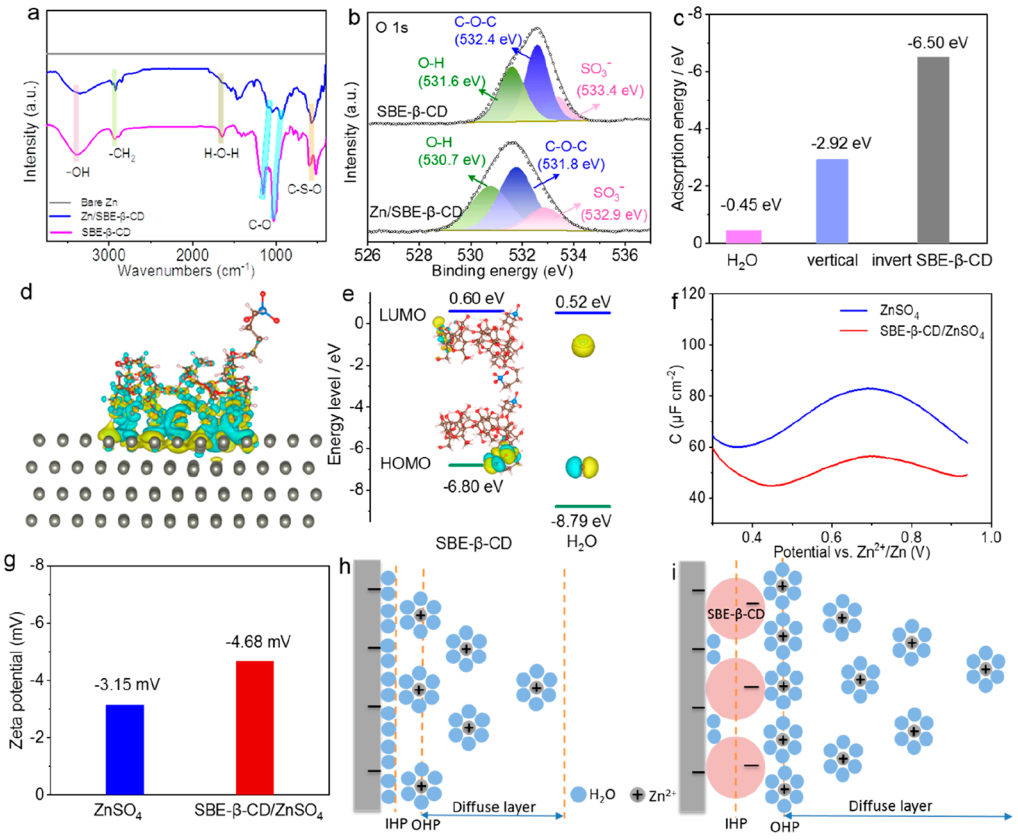

Figure 1. (a) FTIR spectra of pristine Zn plate (gray), Zn plate after immersion in electrolyte with SBE-β-CD additive (blue), and SBE-β-CD powder (pink). (b) The high-resolution O 1s region in XPS spectra of SBE-β-CD powder (top) and dry Zn plate after immersion in SBE-β-CD aqueous solution (bottom). (c) The adsorption energy of H_2O, and SBE-β-CD anions on Zn (0002) surface, insets are the corresponding absorption models for different states. (d) The charge density difference of Zn (0002) with H_2O and invert-placed SBE-β-CD adsorption (yellow and cyanine semitransparent clusters represent increase and decrease of electron density, respectively). (e) LUMO, HOMO isosurfaces of H_2O molecules (left), and SBE-β-CD (right). (f) The Zeta potentials of Zn depositions measured in aqueous $ZnSO_4$ electrolyte and SBE-β-CD/$ZnSO_4$ electrolyte. (The deposited Zn metal were collected from the Ti electrode of the Zn//Ti cell after discharging 1 h at the current density of 2 mA cm^{-2}.) (g) The differential capacitance curves of Zn//Cu cell in the electrolytes with or without SBE-β-CD additive. Schematic illustration of EDL structure in electrolyte (h) without and (i) with SBE-β-CD anion.

high fields after 2 M $ZnSO_4$ was added to the 5 mM SBE-β-CD electrolyte (Figure S4b). The conclusion is consistent with our previous studies on ion clustering in aqueous solutions:[30] the ~0.005 M anion (total number of negative charge) of SBE-β-CD cannot compete with the much stronger and more concentrated (2M) SO_4^{2-} or many more (>50M) water molecules to bind to the strongly hydrated Zn^{2+}.

Peaks of the SBE-β-CD in the range from 400 to 3800 cm^{-1} appear in the FTIR spectrum of the Zn foil after immersion in the SBE-β-CD aqueous solution. Moreover, almost all the groups of SBE-β-CD anions are affected (Figures 1a and S5), indicative of the chemadsorption of SBE-β-CD on the Zn metal surface. The XPS results in Figure 1b reveal more detail about the interaction between functional groups of SBE-β-CD and the Zn metal. After immersion, the O 1s signal shifts to lower binding energies due to the reduced electron density around O, among which the peak assigned to -OH shifts most obviously, implying the direct interaction between -OH and Zn.[31] The adsorption of -OH on Zn also leads to the deformation of the framework of SBE-β-CD, accounting for the chemical shift of -C-O-C-. The red shift of -SO_3^- signal confirms the chemical adsorption of -SO_3^- on Zn. The -C-OH/-C-S signal in C 1s spectra greatly decreases, further verifying the interaction between Zn and -OH (Figure S6).

The strong interaction between the Zn surface and SBE-β-CD is further confirmed by density functional theory (DFT) calculations. As shown in Figure 1c, the adsorption energy of SBE-β-CD anions at a vertical state (−2.92 eV) and at an invert state (−6.50 eV) on Zn (0002) is much lower than that of H_2O (−0.45 eV) (Figures S7−S9). Specifically, SBE-β-CD prefers to adsorb on the Zn (0002) facet at an invert state based on the higher E_{ads} of the invert state than the vertical state (−6.50 eV versus −2.92 eV). Several oxygen atoms play a connecting role in the ring structure of SBE-β-CD anions. Thus, the actual number of binding sites of SBE-β-CD anion on Zn metal are only 12 rather than 41. As a result, the binding energy per oxygen of SBE-β-CD anion is calculated to be -0.54 eV (−6.5 eV/12), which is larger than that (−0.45 eV) of per oxygen of H_2O. In addition, the adsorption process of supramolecular SBE-β-CD anion with large volume is synergistic. Hence, when normalized by the number of oxygen atoms, the adsorption energy of SBE-β-CD anions at an invert state (−6.50 eV) of SBE-β-CD is lower than that of H_2O, indicating SBE-β-CD anions preferentially adsorb on the Zn anode and thus isolate H_2O adsorption to block side reactions on the Zn surface. The differential charge density distribution of the optimized adsorption configurations shows that the electron cloud between Zn atoms and the O atoms is overlapped in the Zn (0002)-vertically placed SBE-β-CD

https://doi.org/10.1021/acsnano.3c03220
ACS Nano 2023, 17, 24619−24631

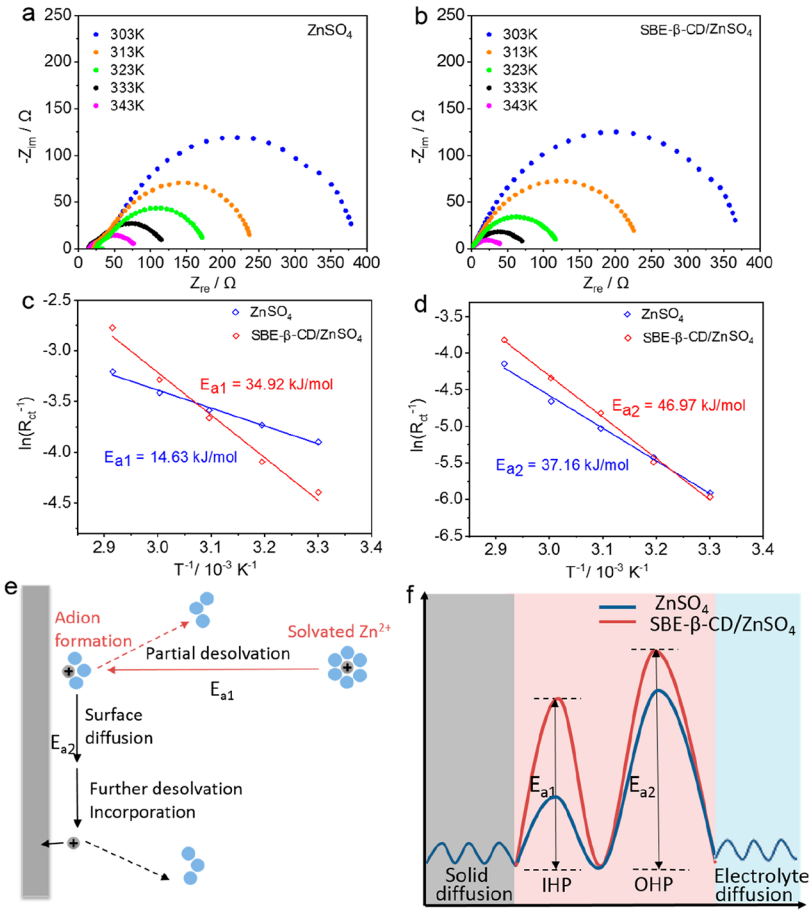

Figure 2. Nyquist plots of Zn//Zn cells at different temperatures in (a) $ZnSO_4$ electrolyte and (b) SBE-β-CD/$ZnSO_4$ electrolyte. (c) and (d) Arrhenius behavior and comparison of activation energies between the R_1 and R_2 derived from Nyquist plots of Zn//Zn cells in $ZnSO_4$ electrolyte without and with SBE-β-CD additive. (e) Schematic representation of the electrocrystallization of a solvated Zn^{2+} onto Zn substrate. (f) Correlation of the energy barrier of Zn^{2+} in the inner Helmholtz plane (IHP) and outer Helmholtz plane (OHP). The initial OHP mainly influences E_{a1}, while E_{a2} is determined by the initial IHP.

anion model (Figure 1d), whereas there is hardly a shared electron in the Zn (0002)-H_2O model (Figure S7c). The frontier molecular orbital theory can provide insight into the interaction between frontier orbitals (HOMO and LUMO) of SBE-β-CD and Zn metal. The higher value of E_{HOMO} and the lower value of E_{LUMO} indicate the tendency of the molecule to donate and accept electrons, respectively. Figure 1e compares the localization of HOMO and LUMO of SBE-β-CD and H_2O. The higher HOMO energy level of SBE-β-CD than that of H_2O (−6.80 eV versus −8.79 eV) suggests a better electron donating ability of SBE-β-CD. Thus, unoccupied orbitals of Zn atom prefers to accept electrons from SBE-β-CD rather than H_2O to form coordinate bonds, suggesting the occurrence of chemisorption. Chemisorption is a kind of adsorption that involves a chemical reaction between the surface and the adsorbate. However, not all chemical reactions are redox reactions. To investigate whether the redox reaction between SBE-β-CD and Zn occur, cyclic voltammograms of Zn//Ti cells in SBE-β-CD/$ZnSO_4$ electrolyte were carried out. The cyclic voltammograms (CVs) profiles of Zn//Ti cells in SBE-β-CD/$ZnSO_4$ electrolyte at a scan rate of 0.5 mV s^{-1} in the voltage range of −0.2 to 2.1 V shows a pair of redox peaks that correspond to Zn stripping/plating (Figure S10), revealing a similar redox behavior with that of cells with $ZnSO_4$ electrolyte. Moreover, the redox peak positions almost remain unchanged, and there is not any other oxidation peak with the increasing cycle, indicating SBE-β-CD does not undergo redox reaction, or decompose and form an SEI in the electrochemical window. In addition, the calculated oxidation potentials for SBE-β-CD on Zn surface (~1.68 V (vs. SHE)) are higher than oxygen evolution potential, which is consistent with the experimental result. Thus, the interaction between SBE-β-CD and Zn is chemisorption rather than a redox reaction. Moreover, SBE-β-CD anions appear not to desorb from Zn electrode surface when Zn electrode is negatively polarized (Figures S11 and 12).

Alternating current (AC) voltammetry is employed to investigate the capacitance change and the EDL structure evolution after introducing the SBE-β-CD additive. The capacitance obtained in SBE-β-CD/$ZnSO_4$ electrolyte is significantly lower than that of the bare electrolyte (Figure 1f), implying different adsorbed species in the IHP. The potential of zero charge (PZC) refers to the potential at which no excess charge exists on surface and describes the condition when the capacitance on a surface is minimum, which is adopted as an indicator for the EDL structure evolution.[32] The value of the PZC shifts positively with the addition of SBE-β-CD, indicating the specific adsorption of SBE-β-CD anions in the IHP. The Zn deposits obtained from bare electrolyte show a Zeta potential of ~ −3.15 mV (Figure 1g), revealing that the Zn deposits are negatively charged. While the Zeta potential of the Zn deposits decreases to about −4.68 mV after introducing

https://doi.org/10.1021/acsnano.3c03220
ACS Nano 2023, 17, 24619−24631

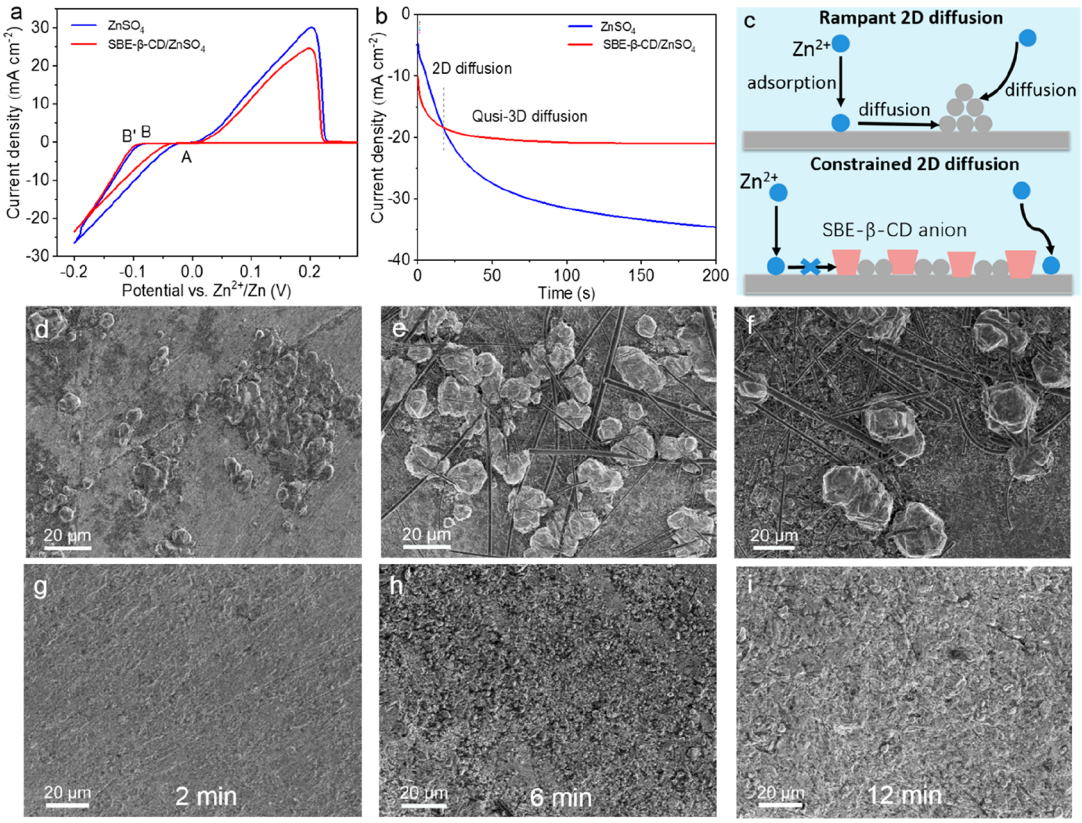

Figure 3. (a) Cyclic voltammograms (CVs) profiles for Zn nucleation in SBE-β-CD/$ZnSO_4$ and $ZnSO_4$ electrolyte at a scan rate of 1 mV s^{-1}. (b) Chronoamperometry curves at a constant overpotential of −150 mV for electroplating Zn in SBE-β-CD/$ZnSO_4$ and $ZnSO_4$ electrolyte. (c) Schematics of the Zn^{2+} diffusion and reduction processes on Zn electrodes in $ZnSO_4$ electrolyte with and without the SBE-β-CD additive. SEM images of Zn anode after deposition at 5 mA cm^{-2} for 2 min, 6 and 12 min (d–f) in $ZnSO_4$ electrolyte and (g–i) in SBE-β-CD/$ZnSO_4$ electrolyte.

SBE-β-CD in the electrolyte, suggesting more net charges on the surface of Zn deposits due to the adsorption of SBE-β-CD anions. The larger radius of SBE-β-CD anion compared to H_2O and more net charges on the surface of Zn with the presence of SBE-β-CD anions in the IHP induce the formation of a thicker EDL structure (Figure 1h,i). The potential drop within the EDL in the SBE-β-CD/$ZnSO_4$ electrolyte is smaller than that in bare electrolyte due to larger thickness and higher PZC potential.[33] It is well-known that even a very small potential drop in EDL can lead to a large gap in electric field due to the thin thickness of EDL (~0.2–20 nm). Hence, the huge electric field gradient in the EDL in the bare electrolyte renders concentrated Zn-ion flux and fast Zn^{2+} transfer, which triggers uneven Zn deposition and the rapid formation of Zn dendrites. In contrast, the small electric field gradient within the EDL in SBE-β-CD/$ZnSO_4$ electrolyte is favorable for homogenizing Zn^{2+} flux and slowing down Zn^{2+} transfer rate, eventually leading to even Zn deposition.

To investigate the effect of the structure of DEL on the dynamical behavior of Zn^{2+} transport at the electrode–electrolyte interface, electrochemical impedance spectroscopy (EIS) measurements are carried out at various temperature. As displayed in Figure 2a,b, there are two semicircles in SBE-β-CD/$ZnSO_4$ and $ZnSO_4$ electrolyte. The simulated equivalent circuit models (Figure S13) are constructed based on the as-obtained EIS profiles. In the equivalent circuit, R_s, R_1 and R_2 represent the series resistance, interfacial charge transfer resistance at high frequency (from 1 Hz to 100 kHz) range, and interfacial charge transfer resistance at low frequency (from 10 mHz to 1 Hz) range, respectively. The cell in SBE-β-CD/$ZnSO_4$ electrolyte shows higher interfacial charge transfer resistances (R_{ct}) value (66 Ω, 370 Ω) than those in $ZnSO_4$ electrolyte (45 Ω, 306 Ω), revealing SBE-β-CD effectively impeding Zn^{2+} transport. Moreover, the charge-transfer process is temperature dependent. The relationship between R and T is in line with the Arrhenius equation. By fitting log (R_{ct}^{-1}) versus 1000/T, the activation energy (E_a) of Zn^{2+} transport is computed (Figure 2c,d).

The adatom model has been extensively used to depict the processes of metal deposition and the Li-ion insertion mechanism. According to the adatom model,[34,35] the Zn^{2+} deposition at the Zn/electrolyte interface can be divided into two processes (Figure 2e). One is the Zn^{2+} transfer between the Outer Helmholtz Plane (OHP) and Inner Helmholtz Plane (IHP), including the partial desolvation of Zn^{2+} and the ad-ion formation at the Zn/electrolyte interface. The other is the Zn^{2+} transfer between the IHP and electrode, involving the ad-ion diffusion across the electrode surface, further desolvation and incorporation reaction of Zn^{2+} into the host lattice. Correspondingly, R_1 at the high frequency and R_2 at the low frequency can be attributed to the charge transfer resistance between the OHP and IHP, and between the IHP and electrode, respectively.[36] There is a distinct increase in the activation energy (E_{a1}) of Zn^{2+} transfer between the OHP and IHP (from 14.63 kJ mol^{-1} to 34.92 kJ mol^{-1}) with the presence of SBE-β-CD in IHP (Figure 2c), suggesting the thicker stern layer arising from the adsorption of SBE-β-CD inhibits the desolvation of Zn^{2+} and the ad-ion formation. The

https://doi.org/10.1021/acsnano.3c03220
ACS Nano 2023, 17, 24619–24631

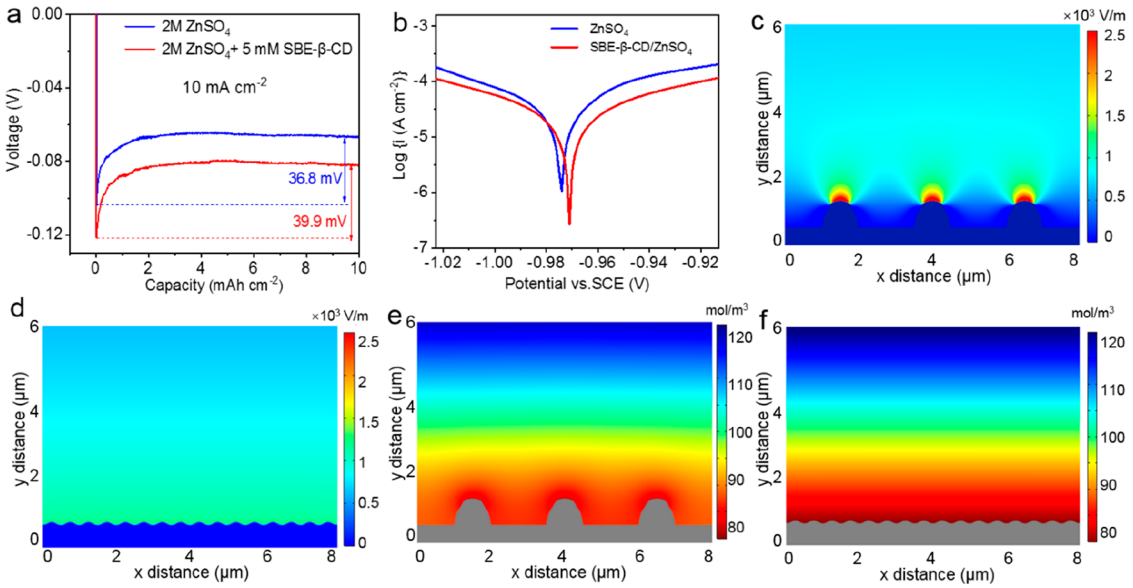

Figure 4. (a) Nucleation overpotential of Zn//Cu cells in 2 M $ZnSO_4$ electrolytes with and without SBE-β-CD additive. (b)The linear polarization curves in SBE-β-CD/$ZnSO_4$ and $ZnSO_4$ electrolyte. Simulations of the electric field distribution of the Zn electrode with (c) $ZnSO_4$ electrolyte and (d) SBE-β-CD/$ZnSO_4$ electrolyte. Simulated Zn^{2+} concentration field distributions on a Zn electrode with (e) $ZnSO_4$ electrolyte and (f) SBE-β-CD/$ZnSO_4$ electrolyte.

activation energy (E_{a2}) of Zn^{2+} transfer between IHP and electrode in SBE-β-CD/$ZnSO_4$ electrolyte (46.97 kJ mol^{-1}) is also larger than that in bare electrolyte (37.16 kJ mol^{-1}) (Figure 2d), suggesting the occupation of SBE-β-CD on the Zn surface impedes the ad-ion diffusion, further desolvation, and lattice incorporation. In summary, the adsorption of SBE-β-CD in the IHP effectively reduces the Zn^{2+} deposition kinetics (Figure 2f), thus favoring uniform Zn^{2+} deposition.

Effect of EDL Structure on Zn Deposition Behavior. In general, the initial nucleation behavior is a critical factor that dictates the morphology of an electrodeposited metal. To reveal the difference in nucleation behavior in the electrolyte with and without the SBE-β-CD additive, cyclic voltammetry (CV) tests of Zn//stainless steel (Zn//SS) half cells in two different electrolytes are conducted (Figure 3a). The potential difference between the initial electroreduction potential of Zn^{2+} at point "B/B′" and the crossover potential at point "A" is defined as the nucleation overpotential (NOP) for Zn^{2+} deposition on a SUS substrate.[37] The relationship between the critical Zn nucleus radius (r_{crit}) in a specific direction and NOP can be described as the following equation:[38]

$$r_{crit} = \frac{2\Upsilon V_m}{F|\eta|} \quad (1)$$

where r_{crit} is the critical Zn nucleus radius in a specific direction, Υ is the surface energy of the Zn-electrolyte interface in the specific direction, V_m is the molar volume of Zn, F is the Faraday's constant, and η is the nucleation overpotential. According to the above equation, the higher the nucleation overpotential (NOP) is, the smaller the nucleus radius is. As shown in Figure 3a, it is obvious that the introduction of an additive increases the NOP value and reduces the cathodic process area, revealing the suppression of electrocrystallization.

Since it is assumed that a rise in current during potentiostatic electrodeposition results from an increase in effective electrode surface area (the formation of dendrites), chronoamperometry (CA) is conducted to further scrutinize the effects of SBE-β-CD additive on the inhibition of Zn nucleation behavior. Figure 3b shows the variation in current versus time of Zn//Zn cells with/without additives at a constant cathodic overpotential of −150 mV within a duration of 200 s. The currents rapidly increase in both cells with/without SBE-β-CD additive during the initial 10s, corresponding to the rampant 2D diffusion nucleation process. The absorbed Zn^{2+} ions tend to diffuse laterally along the surface and aggregate into dendrites to minimize the surface energy and exposed area. In the subsequent deposition in bare electrolyte, the monotonically increasing current indicates the continuous lateral diffusion of Zn^{2+} ions, resulting in the increase of the effective electrode area and the dendritic Zn formation dendrites eventually. In contrast, the current remains almost stable after 60 s in electrolyte with additive, suggesting that 2D diffusion proceeds to the end due to the constrained effect of SBE-β-CD anions on the Zn^{2+} diffusion. The absorbed SBE-β-CD anions on the Zn anode surface provide a higher energy barrier, resulting in even and slower deposition of Zn^{2+}.

SEM images provide direct proof for the distinct nucleation behavior in Zn//Zn cells with/without the SBE-β-CD additive. In the bare electrolyte, there emerges randomly dispersed Zn particles with a diameter of several micrometers at the initial nucleation stage (Figure 3d) due to poor hydrophilicity of Zn and uneven Zn surface. With the increasing deposition time, Zn^{2+} rapidly aggregates on the tips of Zn protrusions driven by enhanced electric field intensity, resulting in further protrusion amplification. After 12 min, the diameter and height of the Zn protrusions reach ∼30 μm (Figure 3f). In contrast, the smaller Zn nuclei uniformly distribute on the surface of Zn metal (Figure 3g−i) without the formation of obvious Zn protrusions with the aid of the SBE-β-CD additive. Benefiting from even electric field intensity at the vicinity of Zn depositions, the superfilling phenomenon take place as the deposition goes on. As a result, the interconnected and compact deposition layer evolves.

https://doi.org/10.1021/acsnano.3c03220
ACS Nano 2023, 17, 24619−24631

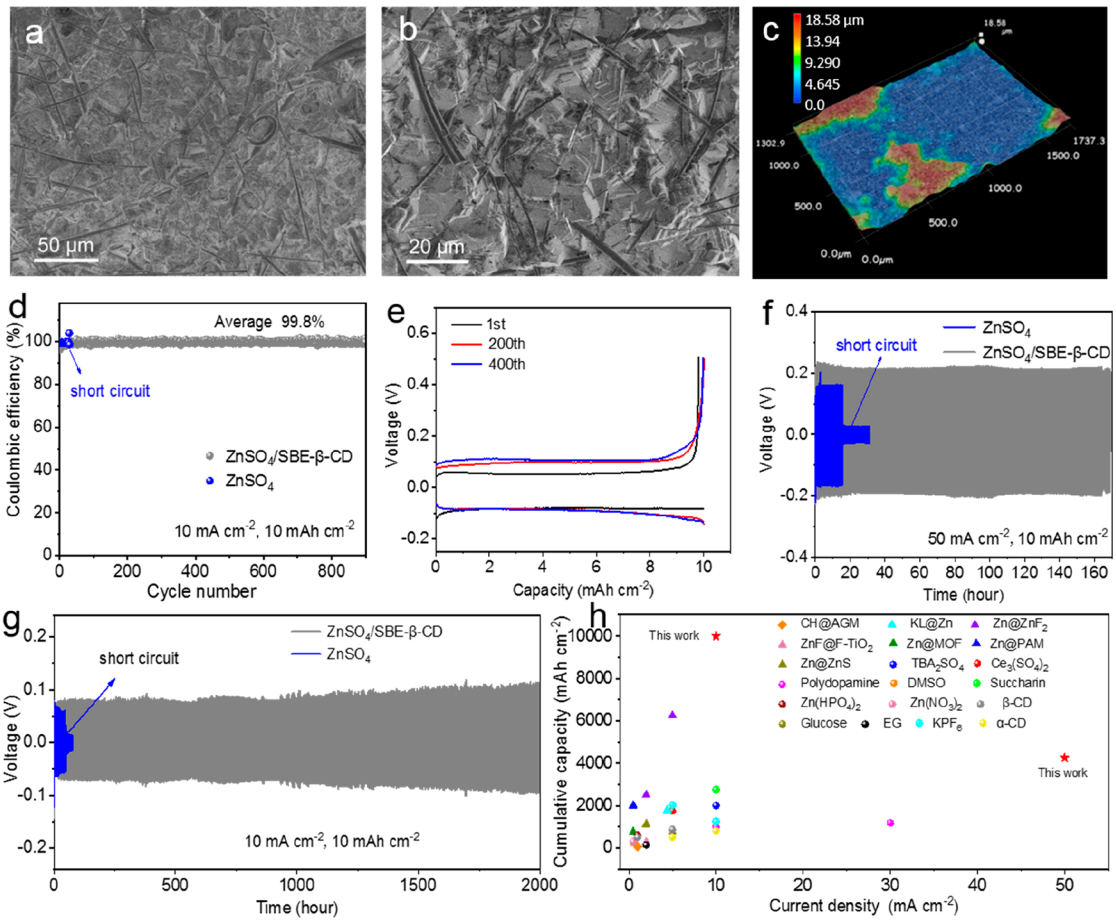

Figure 5. (a),(b) SEM images and (c) LCSM image of Zn deposits at a current density of 10 mA cm^{-2} for a capacity of 10 mA h cm^{-2} in SBE-β-CD/ZnSO$_4$ electrolyte. (d) Coulombic efficiency of Zn plating/stripping in Zn//Cu cells in different electrolytes at 10 mA cm^{-2} and 10 mAh cm^{-2}. (e) Voltage profiles of Zn plating/stripping at selected cycles in Zn//Cu cells with the SBE-β-CD/ZnSO$_4$ electrolyte. The voltage profiles of galvanostatic Zn plating/stripping in Zn//Zn symmetrical cells (f) at a current density of 50 mA cm^{-2} and a capacity of 10 mAh cm^{-2} and (g) at a current density of 10 mA cm^{-2} and a capacity of 10 mAh cm^{-2}. (h) Comparison of cumulative capacity of Zn symmetric cells using the SBE-β-CD/ZnSO$_4$ electrolyte with other reported literature.

The nucleation overpotential at 10 mA cm^{-2} on the Cu substrate increases from 36.8 to 39.9 mV after introducing SBE-β-CD additive (Figure 4a), suggesting the inhibition of Zn nucleation. Experimental results and theoretical calculation both confirm that SBE-β-CD anions do not decompose during electrochemical cycle. Hence, the increased nucleation overpotential after introducing SBE-β-CD additive can be attributed to the resistance stemming from the preferential adsorption of supramolecular SBE-β-CD anion. Linear polarization experiments are performed to investigate the effect of additive on the Zn corrosion. As shown in Figure 4b, the Zn electrode in SBE-β-CD/ZnSO$_4$ electrolyte exhibits a higher corrosion potential (−0.970 V) than that in the bare electrolyte (−0.974 V), suggesting less tendency of corrosion reactions due to the blocking effect of the adsorbed SBE-β-CD anions on the surface of the Zn electrode. Moreover, the reduced corrosion current from 565.8 μA cm^{-2} to 137.1 μA cm^{-2} after introducing additive in electrolyte indicates a lower corrosion rate of the Zn electrode. Moreover, introducing SBE-β-CD into the electrolyte can also suppress the electrochemical water decomposition, as evidenced by the reduced current for hydrogen evolution reaction. The reduction current reduced from −18 to −13 μA at −0.15 V (vs Zn/Zn^{2+}) (Figure S14), demonstrating the absorbed SBE-β-CD layer on Zn surface can act as a barrier to isolate Zn metal from H_2O, which inhibits interfacial side reactions effectively.

The electric field distribution and Zn^{2+} flux distribution at the Zn anode/electrolyte interface mainly dictates the Zn^{2+} deposition behavior and nucleation. To investigate the effect of SBE-β-CD on regulating the interfacial electric field and Zn^{2+} concentration field, a finite element simulation is implemented based on the COMSOL Multiphysics software. As shown in Figure 4c, the protuberances of a bare Zn electrode exhibit inhomogeneous and enhanced electric field intensity, leading to charge accumulation and vertical Zn^{2+} deposition on the tips. Driven by the self-accelerating tip effect, these protuberances eventually evolve into irregular dendrites, resulting in shortcircuits and premature failure of batteries. SBE-β-CD preferentially adsorbs on the protrusion of zinc deposits due to the locally high electron density. Since SBE-β-CD is an insulating material, the adsorption of SBE-β-CD on Zn nuclei can lower the local electric field intensity from ∼2400 V m^{-1} to ∼1100 V m^{-1} (Figure 4c,d), and thus suppress the growth of Zn dendrite from the Zn bud and promote the Zn^{2+} deposition in the vicinity of buds.

The surface wettability of the electrode is of great importance for ion transfer at the electrolyte/electrode interface. The sessile drop contact angle is measured to

https://doi.org/10.1021/acsnano.3c03220
ACS Nano 2023, 17, 24619−24631

evaluate the wettability of the Zn metal. As illustrated in Figure S15, the contact angle of the Zn electrode with SBE-β-CD/$ZnSO_4$ electrolyte (67.2°) is smaller than that with bare eletrolyte (79.8°), demonstrating the improved hydrophilicity of Zn electrode. According to the Extrand's model,[39] the variation in the wetting free energy (ΔG) with/without additive is calculated by the below equation:

$$\Delta G = \frac{RT}{3}\ln\frac{(1-\cos\theta_a)^2(2+\cos\theta_a)}{4} \quad (2)$$

where θ_a is the contact angle, R is the ideal gas constant, and T is the absolute temperature. The value decreases from −824.3 J mol^{-1} to −1235.9 J mol^{-1} after introducing the SBE-β-CD additive, indicative of a stronger association between the Zn electrode with electrolyte, which favors an even Zn^{2+} flux. The simulated concentration gradient of Zn^{2+} from the bulk electrolyte to the Zn anode surface becomes smaller (Figure 4e,f). In other words, the Zn^{2+} flux at the interface is much more homogeneous than that of the bare Zn anode. As a result of the constricted vertical growth, a smooth deposition layer with compact and orderly morphology is formed.

Electrochemical Properties of Regulated Zn Anodes. As the SBE-β-CD concentration increases from 0.02 to 0.1 M, the ionic conductivity of the hybrid electrolyte with 0.1 M additive is still up to 51.5 mS cm^{-1} (Figure S16a), which is similar to that of a bare electrolyte. In addition, the addition of 0.002−0.01 M SBE-β-CD exerts little influence on the pH value of the $ZnSO_4$ electrolyte (Figure S16b). To find the optimal concentration of SBE-β-CD, electrochemical tests of the cells with different contents of SBE-β-CD are carried out. The Zn//Cu cell with 0.005 M SBE-β-CD additive shows a higher average CE of ∼99.2% compared to other counterparts (Figure S17) at a high current density of 5 mA cm^{-2} with a high areal capacity of 5 mAh cm^{-2}. Moreover, a lifespan of 2000 h is achieved with 0.005 M SBE-β-CD, suggesting that the reversibility of Zn chemistry is significantly improved (Figure S18). However, excess SBE-β-CD NE (>0.01 M) renders a shorter cycle life, which can be attributed to the increased polarization with higher SBE-β-CD contents. Excessive SBE-β-CD (>0.01 M) can greatly increase the activation energy of Zn^{2+} transfer at the interface of Zn electrode and electrolyte, resulting in a large polarization, which can reduce the reversibility of Zn stripping/plating. As a result, dead Zn and Zn dendrites gradually aggregate on the surface, thus shortening the cycle life. Taking into consideration the balance between cycling life and polarization, the optimized SBE-β-CD additive concentration is 0.005 M.

In the bare electrolyte, agglomerate-like dendrites appear on the Zn surface after 1 h of plating at 10 mA cm^{-2}(Figures19a,b and S20a). Zn^{2+} tends to aggregate on the tips due to the strong electrical field and concentrated Zn^{2+} flux at the tips. In contrast, the Zn depositions layer in SBE-β-CD/$ZnSO_4$ electrolyte is compact and homogeneous (Figures 5a,b and S20b), indicating much more homogeneous Zn nucleation and deposition with the aid of SBE-β-CD additive. The roughness of the Zn surface is further examined by laser confocal scanning microscope (LCSM). There are large protrusions with ∼69.91 μm height in $ZnSO_4$ electrolyte (Figure S19c), whereas the Zn deposit (the height difference of ∼18.58 μm) is much flatter and more compact due to numerous and fine zincophilic nucleation sites with the presence of SBE-β-CD in the electrolyte (Figure 5c). X-ray diffraction (XRD) spectra of the deposited Zn at a current density of 10 mA cm^{-2} for a capacity of 10 mA h cm^{-2} in electrolyte with SBE-β-CD anion additive (Figure S21) show the intensity of Zn (002) diffraction significantly increases, which is comparable to that of (101) diffractions, implying the crucial role of the SBE-β-CD anion in regulating the preferred crystal plane growth and compact electrodeposition.

To evaluate the effect of the SBE-β-CD additive on the reversibility and stability of the metallic Zn anode, we perform a series of plating/stripping measurements under galvanostatic condition. The Coulombic efficiency (CE) is a critical indicator for evaluating the reversibility and stability of the Zn plating/stripping process. The Zn//Cu coin-type cells using Zn foil as anode and Cu foil as cathode are employed to examine the CE of Zn plating/stripping at a high current density of 10 mA cm^{-2} with an areal capacity of 10 mA h cm^{-2}. The Zn//Cu cells cycled in the SBE-β-CD/$ZnSO_4$ electrolyte shows a high average CE of 99.8%, whereas the CEs of their counterparts in the $ZnSO_4$ electrolyte fluctuate rapidly after only 15 cycles with a low average CE of ∼90.7% due to dendrite formation and/or parasitic reactions (Figure 5d). Figure 5e exhibits the corresponding charge−discharge voltage profiles at selected cycles of the Zn//Cu cells. The cells deliver a steady overpotential of ∼24 mV over 4000 cycles without showing any trend toward deterioration, manifesting exceptional reversibility of Zn plating/stripping in cells with SBE -β-CD additive.

As shown in Figure 5g, after introduction of SBE-β-CD into the electrolyte, the Zn symmetric cells can be operated steadily for ∼2000 h at a high current density of 10 mA cm^{-2} with a capacity of 10 mAh cm^{-2}, whereas cells in normal electrolyte fail suddenly after only 30 h. When cycled at an elevated current density of 50 mA cm^{-2} with a high capacity of 10 mAh cm^{-2}, the Zn symmetric cells with the SBE-β-CD additive in the electrolyte can still achieve a long cycle lifespan of 170 h (Figure 5f). In sharp contrast, the Zn symmetric cells in bare electrolyte show a poor cycle stability of ∼18 h. The SBE-β-CD additive also exerts a positive effect on the reversibility and stability of the Zn plating/stripping at a low current density (Figure S22). The Zn//Cu cell in $ZnSO_4$ electrolyte delivers an average CE of 98.60% over 260 cycles and encounters a short-circuit caused by Zn dendrite formation after 260 cycles at a low current density of 1 mA cm^{-2} with an areal capacity of 0.5 mAh cm^{-2}, accompanied by fluctuant CE after 520h. By contrast, the Zn//Cu cell with a 5 mM SBE-β-CD additive operates stably for over 1640 h and delivers a high average CE of 99.44% over 1000 cycles at the same current density, demonstrating the effectiveness of SBE-β-CD additive.

In galvanostatic cycling, the cumulative capacity, the largest current density, and the areal capacity applied to the Zn anode are proposed as indicators to accurately evaluate the cycle stability of Zn asymmetric cells. Figure 5h shows the cumulative capacity of Zn asymmetric cells in recent reports under mildly acidic conditions at a fixed current density. The Zn symmetric cells with SBE-β-CD additive in our work achieves an ultrahigh cumulative capacity of 10000 and 4250 mAh cm^{-2} at the current density of 10 and 50 mA cm^{-2}, respectively, which is superior to all previously reported values,[16−18,26,27,40−53] demonstrating that our design is capable of meeting the requirements of high areal capacity and long life in practical applications.

Electrochemical Performance of Zn//MnO_2 Full Cells. To demonstrate the reliability of the SBE-β-CD additive

https://doi.org/10.1021/acsnano.3c03220
ACS Nano 2023, 17, 24619−24631

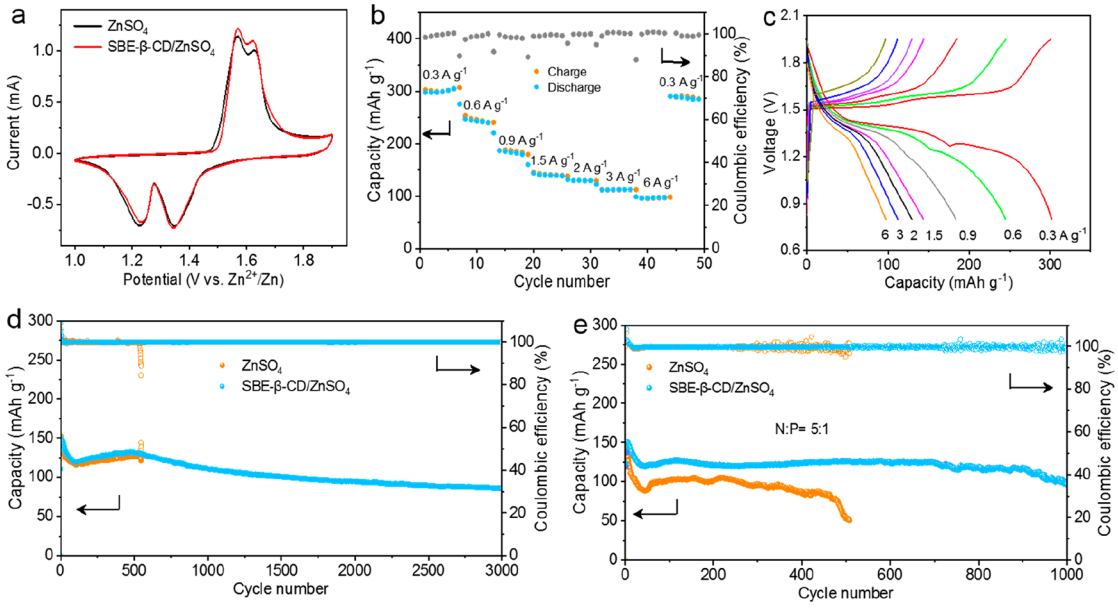

Figure 6. Electrochemical performance of Zn//MnO_2 cells in 2 M $ZnSO_4$ electrolytes with and without the SBE-β-CD additive. (a) CV curves at a scan rate of 0.2 mV s^{-1}. (b) Rate capability in $ZnSO_4$/SBE-β-CD electrolyte. (c) The corresponding charge/discharge curves at various rates. (d) Comparison of the cycling performance at 1 A g^{-1} in two different electrolytes. (e) Comparison of the cycling performance at 1 A g^{-1} with a limited Zn supply (N/P capacity ratio= 5:1).

strategy in practical applications, Zn||MnO_2 full cells are assembled employing 2 M $ZnSO_4$ + 0.2 M $MnSO_4$ electrolyte with/without SBE-β-CD additive. (Noting: 0.2 M $MnSO_4$ is added into $ZnSO_4$ electrolyte to suppress the dissolution of MnO_2 during electrochemical cycling.) The MnO_2 cathode is prepared by a traditional hydrothermal method. The XRD patterns of the sample (Figure S23) show the crystalline phase of α-MnO_2 (JCPDS: 44−0141). The SEM image (Figure S24) displays a homogeneous one-dimensional (1D) nanorod structure with a length of a few micrometers and a diameter of about 50 nm. The CV curves of Zn//MnO_2 full cells in two electrolytes at a scan rate of 0.2 mV s^{-1} (Figure 6a) reveal a similar redox behavior with one oxidation peak and two reduction peaks, corresponding to the consequent H^+ and Zn^{2+} intercalation mechanism, which indicates the SBE-β-CD additive did not affect the redox reactions in the MnO_2 cathode.

The Zn//MnO_2 cell with SBE-β-CD additive delivers a high capacity of 298.9 mAh g^{-1} at 1 C (1C = 308 mAh g^{-1}) similar to that of the Zn//MnO_2 cell with bare electrolyte (301.2 mAh g^{-1}) (Figures 6b and S25). Their charge/discharge curves display similar charge/discharge platforms at 1.27 and 1.57 V, consistent with the redox peaks of the CV curves (Figures 6c and S25). When the current density increases to 0.6, 0.9, 1.5, 2, 3, and 6 A g^{-1}, the capacity of Zn//MnO_2 cells decreases to 246.7, 186.4, 143.4, 129.9, 111.4, and 96.8 mAh g^{-1}, respectively. When the rate suddenly shifted back to the low rate of 0.3 A g^{-1}, the reversible capacities recovered to 290.2 mA h g^{-1}, reflecting the suppression of side reactions and the highly stable Zn anode (Figure 6b).

The long-term cycling stability of the Zn//MnO_2 cells with a high-loading MnO_2 cathode (~8.0 mg cm^{-2}) is further investigated at 1 C in both electrolytes (Figure 6d). In bare electrolyte, the Zn//MnO_2 cells encounter a sudden short-circuit and fail in fewer than 520 cycles. In contrast, the Zn//MnO_2 cells with the SBE-β-CD additive achieve a long life over 3000 cycles with a capacity retention of 78.1%. The capacity gradually increases during the initial stage, and rapidly decreases in the following cycles, and then slightly increases, and slowly decreases at the final stage, which is very common for Zn//MnO_2 batteries in the $ZnSO_4$ + $MnSO_4$ electrolyte.[54,55] The capacity increase during the initial six cycles stems from the gradual activation of electrodes. The subsequent rapid capacity attenuation between the 10th and 120th cycle can be attributed to the dissolution of Mn^{2+} resulted from Mn^{3+} disproportionation into the electrolyte. The increase of Mn^{2+} content in electrolyte arising from the dissolution of Mn^{2+} changes the equilibrium between Mn^{2+} dissolution and the reoxidation of Mn^{2+} in the electrolyte. This significantly suppresses continuous Mn^{2+}dissolution and promotes electrochemical deposition of MnO_2, leading to a gradual capacity increase during the following cycles (from the 120th to 500th cycle).[54] The Zn^{2+} insertion is less reversible than that of H^+, which leads to increased amount of irreversible $ZnMn_2O_4$ in the cathode with the increasing cycles, accounting for the capacity fading at the last stage.[55] Furthermore, the cycling performance of Zn//MnO_2 cells is tested under the harsh condition of a limited Zn supply (11.6 mAh cm^{-2}, 20 μm thick) and a high-loading MnO_2 cathode (8.0 mg cm^{-2}). As shown in Figure 6e, the full cells with N/P = 5:1 in bare electrolyte suffer from fast capacity degradation during 500 cycles due to the poor utilization caused by side reactions and formation of the Zn dendrites. In contrast, the cells with SBE-β-CD additive exhibit greatly improved cycling stability with Coulombic efficiency approaching 99.3% and high capacity retention of 80% for 1000 cycles, validating the SBE-β-CD additive could effectively suppress detrimental Zn dendrites and side reactions to promote the reversibility of Zn plating/stripping.

All major electrochemical results have statistics $N \geq 3$ and are repeatable in our experiments.

https://doi.org/10.1021/acsnano.3c03220
ACS Nano 2023, 17, 24619−24631

CONCLUSION

In summary, the interfacial chemistry on Zn anode is successfully regulated by changing the EDL structure with the adsorption of supramolecular cyclodextrin anions in IHP. The absorption of the anions increases the charge transfer activation energy for Zn^{2+} to go through the OHP (Ea_1) and IHP (Ea_2) and thus slows down the Zn^{2+} transfer kinetics and homogenizes the Zn^{2+} flux in the proximity of the Zn metal surface, resulting in a dense and even Zn electrodeposition. Benefiting from the improved interfacial stability, the cycle life of Zn||Zn cells is prolonged to over 1000 cycles at a high current density of 10 mA cm^{-2} with a high capacity of 10 mAh cm^{-2} with an average Coulombic effiffifficiency of 99.5%, achieving ultrahigh cumulative capacity of 10000 and 4250 mAh cm^{-2} at a respective current density of 10 and 50 mA cm^{-2}. Moreover, the full battery coupled with the high-loaded MnO_2 cathode (~8 mg cm^{-2}) achieves long cycling stability over 3000 cycles at a high rate of 1.0 A g^{-1}.

EXPERIMENTAL SECTION

Preparation of α-MnO_2 Cathode and Zn Anode. Six mmoL of $KMnO_4$ was dissolved in 60 mL of deionized water, and then 20 mmol of concentrated HCl was slowly added into the solution under vigorous stirring. The mixture was stirred vigorously at room temperature for several minutes until a transparent purple solution was obtained. The above solution was then transferred to a Teflon-lined stainless steel autoclave and heated to 140 °C and maintained for 12 h. After cooling, the precipitates was collected by centrifugation, washed several times with deionized water, and dried at 60 °C in a vacuum oven overnight. The α-MnO_2 cathodes were prepared by coating the slurry mixture composed of 70 wt % α-MnO_2, 22 wt % carbon black, 4 wt % carboxymethylcellulose, and 4 wt % styrene−butadiene rubber binder on graphite paper. The electrodes were then dried in a vacuum oven under 80 °C for 12 h. The mass loading of α-MnO_2 was adjusted to ~8.0 mg cm^{-2}. Zn foil anode is carefully polished with 1000 mesh sandpaper and ultrasonicated in ethanol for 20 min to remove the passivation layer.

Characterization. The morphologies of the electrodes were characterized by a field emission scanning electronmicroscope (FE-SEM, S4800, Hitachi) along with energy dispersive X-ray spectroscopy (EDX) mapping and a transmission electron microscope (TEM, JEM-2100, JEOL) equipped with energy dispersive spectroscopy (EDS) for elemental analysis. The crystal structure of the electrodes was analyzed by X-ray diffraction (Rigaku Dmax/2400 diffractometer with Cu Kα radiation, 40 kV, 100 mA). X-ray photoelectron spectroscopy (XPS) measurements were performed on an X-ray photoelectronspectrometer (Axis Ultra, Kratos Analytical Ltd.). All XPS spectra were calibrated with respect to the C 1s peak binding energy of 284.8 eV. Attenuated total reflection Fourier transform infrared (ATR-FTIR) mapping was performed on a Spectrum Spotlight 200 FT-IR microscope equipped with an ATR sampling universal accessory (PerkinElmer).The ion conductivity of different electrolytes was collected on a conductivity meter (Thermo Fisher Scientific, STAR A112).

Electrochemical Test. The electrochemical performances of the Zn//Zn symmetric cell, Ti//Zn, Cu//Zn asymmetric cell, and α-MnO_2//Zn full cell were evaluated by using CR2032 coin-type cells assembled in air. Symmetric cells were assembled using two identical zinc plates with a diameter of 10 mm and a thickness of 100 μm. The electrodes were separated by glass fiber separators. 2 M $ZnSO_4$ aqueous solution with and without SBE-β-CD additive was used as the typical liquid electrolyte. Full cells were assembled using α-MnO_2 cathode and zinc plates anode (with a thickness of 100 μm, 20 μm), and 2 M $ZnSO_4$ + 0.2 M $MnSO_4$ aqueous electrolyte with and without SBE-β-CD additive.

Cyclic voltammetry (CV) measurements and electrochemical impedance spectroscopy (EIS), linear sweep voltammetry (LSV), linear polarization, and chronoamperograms were carried out on a CHI760C electrochemical workstation. The Zn plating/stripping tests were performed in Zn symmetrical cells in the 2 M $ZnSO_4$ electrolyte with and without SBE-β-CD additive. Coulombic efficiency (CE) measurements were carried out using asymmetrical Cu//Zn cells. The linear polarization measurements were conducted in a three-electrode configuration, where Zn was used as the working electrode, Pt was used as the counter electrode, and saturated calomel (SCE) was used as the reference electrode, respectively.

DFT Calculation Method. Density function theory calculations were performed by using the CP2K package.[56] PBE functional[57] with Grimme D3 correction[58] was used to describe the system. Kohn−Sham DFT was used as the electronic structure method in the framework of the Gaussian and plane waves method.[59,60] The Goedecker−Teter−Hutter (GTH) pseudopotentials,[61,62] DZVP-MOLOPT-GTH basis sets[59] were used to describe the molecules. A plane-wave energy cutoff of 500 Ry has been employed. All the simulation has been carried out within a 13.65 × 15.76 × 353 box underperiodic boundary condition. On the Z direction, there is about 15 Å vacuum to decouple the interaction between the images. A four-layer Zn (0002) surface has been used to model the surface, and the bottom two layers are kept fixed to maintain the bulk property.

Finite Element Method Simulations. The simulations of electric fields and Zn^{2+} concentration field distributions at the anode/electrolyte interface were performed using COMSOL Multiphysics software based on the finite element method. A simplified 2D model was established, in which the length of two electrodes is 8.0 μm and the height is 0.5 μm with a distance of 6 μm between them. Deformed geometry interfaces were applied to the anode. Deformed geometry interfaces based on the SEM observation were applied to the Zn anode. The initial concentration of Zn^{2+} was set to be 1.0 mol L^{-1}. The exchange current density was set at 20 A m^{-2}. The voltage hysteresis from symmetric cells is set as the cathodic potential, and the anodic potential is a constant of 0. The contact angles of the Zn electrode with $ZnSO_4$ electrolyte and SBE-β-CD/$ZnSO_4$ electrolyte are 79.8° and 67.2°, respectively. The ion flux was calculated through a 2D Nernst−Planck formulation.

ASSOCIATED CONTENT

Data Availability Statement

All data needed to evaluate the conclusions in the paper are present in the paper and/or the Supporting Information. Additional data related to this paper may be requested from the authors.

Supporting Information

The Supporting Information is available free of charge at https://pubs.acs.org/doi/10.1021/acsnano.3c03220.

Molecular structure of the SBE-β-CD anion; EDS mapping of Zn soaked in SBE-β-CD/$ZnSO_4$ electrolyte; FTIR of electrolytes; HNMR spectra of the different electrolytes; FT-IR spectra/XPS spectra of SBE-β-CD powder and dry Zn plate after immersion in SBE-β-CD aqueous solution; Side view and top view of adsorbed H_2O/adsorbed invert SBE-β-CD anions/vertical SBE-β-CD anions on Zn (0002) surface; CV profiles of Zn//Ti cells in SBE-β-CD/$ZnSO_4$ and $ZnSO_4$ electrolyte; EDS mapping of Zn plate after negative polarization; XPS spectra of SBE-β-CD powder and dry Zn plate after negative polarization; Nyquist plot of Zn//Zn symmetrical battery; HER performance Ti//Zn asymmetric cell; Contact angles test of electrolyte on Zn electrode; Ionic conductivity and pH evolution of 2 M $ZnSO_4$ electrolytes with concentrations of SBE-β-CD additive; Comparison of the Coulombic effciency of Zn plating/stripping in Zn/Cu cells; Cycling stability of Zn||Zn cells in different electrolytes; SEM images and LCSM image

https://doi.org/10.1021/acsnano.3c03220
ACS Nano 2023, 17, 24619−24631

of Zn deposits; Cross-sectional SEM images of Zn deposits; XRD spectra of the deposited Zn; Coulombic efficiency of Zn plating/stripping in Zn/Cu cells at 1 mA cm^{-2} and 0.5 mAh cm^{-2}; XRD patterns of as-prepared α-MnO_2 nanofibers; SEM images of as-prepared α-MnO_2 nanofibers; Galvanostatic charge/discharge curves of Zn//MnO_2 cells at various rates. Supplementary note 1. The differences between this work and other similar works Table S1. Comparison of the cycling stability of Zn//Zn symmetric cells with previous reports (PDF)

AUTHOR INFORMATION

Corresponding Authors

Junrong Zheng − *Beijing National Laboratory for Molecular Sciences, College of Chemistry and Molecular Engineering, Peking University, Beijing 100871, China;* orcid.org/0000-0002-4472-8576; Email: junrong@pku.edu.cn

Jitao Chen − *Beijing National Laboratory for Molecular Sciences, College of Chemistry and Molecular Engineering, Peking University, Beijing 100871, China;* orcid.org/0000-0002-2620-5587; Email: chenjitao@pku.edu.cn

Authors

Lulu Wang − *Beijing National Laboratory for Molecular Sciences, College of Chemistry and Molecular Engineering, Peking University, Beijing 100871, China*

Chengzhen Shen − *Beijing National Laboratory for Molecular Sciences, College of Chemistry and Molecular Engineering, Peking University, Beijing 100871, China*

Chaoran Huang − *Beijing National Laboratory for Molecular Sciences, College of Chemistry and Molecular Engineering, Peking University, Beijing 100871, China*

Complete contact information is available at: https://pubs.acs.org/10.1021/acsnano.3c03220

Author Contributions

[⊥]L.W. and C.S. contributed equally. L.W. and J.Z. designed experiments. C.S. carried out theoretical calculations. C.H. performed finite element method simulations. J.Z. supervised the project. L.W. performed experiments. J.Z., J.C., L.W., C.S., and C.H. discussed experiments and results. L.W. and J.Z. prepared and revised the manuscript.

Notes

The authors declare no competing financial interest.

ACKNOWLEDGMENTS

We thank S. Huang, C. Peng, and J. Ding from the College of Chemistry and Molecular Engineering in Peking University for the support of data analysis. We acknowledge financial support from the National Science Foundation of China (NSFC-21927901, 92261206, 21627805, 12174012, and 21821004), MOST (2016YFB0700604, 2021YFB2400400, 2017YFA0204702, and special talent programs) of China and China Postdoctoral Science Foundation (2022T150004).

REFERENCES

(1) Parker, J. F.; Chervin, C. N.; Pala, I. R.; Machler, M.; Burz, M. F.; Long, J. W.; Rolison, D. R. Rechargeable nickel-3D zinc batteries: An energy-dense, safer alternative to lithium-ion. *Science* **2017**, *356* (6336), 415−418.

(2) Zhang, X. G. Corrosion and Electrochemistry of Zinc. *Br. Corros. J.* **1996**, *32* (1), 28−29.

(3) Kundu, D.; Adams, B. D.; Duffort, V.; Vajargah, S. H.; Nazar, L. F. A high-capacity and long-life aqueous rechargeable zinc battery using a metal oxide intercalation cathode. *Nat. Energy* **2016**, *1* (10), 16119.

(4) Yang, Q.; Liang, G.; Guo, Y.; Liu, Z.; Yan, B.; Wang, D.; Huang, Z.; Li, X.; Fan, J.; Zhi, C. Do Zinc Dendrites Exist in Neutral Zinc Batteries: A Developed Electrohealing Strategy to In Situ Rescue In-Service Batteries. *Adv. Mater.* **2019**, *31* (43), No. 1903778.

(5) Yang, Q.; Li, Q.; Liu, Z.; Wang, D.; Guo, Y.; Li, X.; Tang, Y.; Li, H.; Dong, B.; Zhi, C. Dendrites in Zn-Based Batteries. *Adv. Mater.* **2020**, *32* (48), No. 2001854.

(6) Hao, J.; Li, X.; Zeng, X.; Li, D.; Mao, J.; Guo, Z. Deeply understanding the Zn anode behaviour and corresponding improvement strategies in different aqueous Zn-based batteries. *Energy Environ. Sci.* **2020**, *13* (11), 3917−3949.

(7) Zheng, J.; Archer, L. A. Controlling electrochemical growth of metallic zinc electrodes: Toward affordable rechargeable energy storage systems. *Sci. Adv.* **2021**, *7* (2), No. eabe0219.

(8) Jin, Y.; Han, K. S.; Shao, Y.; Sushko, M. L.; Xiao, J.; Pan, H.; Liu, J. Stabilizing Zinc Anode Reactions by Polyethylene Oxide Polymer in Mild Aqueous Electrolytes. *Adv. Funct. Mater.* **2020**, *30* (43), No. 2003932.

(9) Cao, L.; Li, D.; Hu, E.; Xu, J.; Deng, T.; Ma, L.; Wang, Y.; Yang, X. Q.; Wang, C. Solvation Structure Design for Aqueous Zn Metal Batteries. *J. Am. Chem. Soc.* **2020**, *142* (51), 21404−21409.

(10) Cui, J.; Liu, X.; Xie, Y.; Wu, K.; Wang, Y.; Liu, Y.; Zhang, J.; Yi, J.; Xia, Y. Improved electrochemical reversibility of Zn plating/stripping: a promising approach to suppress water-induced issues through the formation of H-bonding. *Mater. Today Energy* **2020**, *18*, No. 100563.

(11) Xu, W.; Zhao, K.; Huo, W.; Wang, Y.; Yao, G.; Gu, X.; Cheng, H.; Mai, L.; Hu, C.; Wang, X. Diethyl ether as self-healing electrolyte additive enabled long-life rechargeable aqueous zinc ion batteries. *Nano Energy* **2019**, *62*, 275−281.

(12) Deng, C.; Xie, X.; Han, J.; Tang, Y.; Gao, J.; Liu, C.; Shi, X.; Zhou, J.; Liang, S. A Sieve-Functional and Uniform-Porous Kaolin Layer toward Stable Zinc Metal Anode. *Adv. Funct. Mater.* **2020**, *30* (21), No. 2000599.

(13) Yang, H.; Chang, Z.; Qiao, Y.; Deng, H.; Mu, X.; He, P.; Zhou, H. Constructing a Super-Saturated Electrolyte Front Surface for Stable Rechargeable Aqueous Zinc Batteries. *Angew. Chem., Int. Ed.* **2020**, *59* (24), 9377−9381.

(14) Kang, L.; Cui, M.; Jiang, F.; Gao, Y.; Luo, H.; Liu, J.; Liang, W.; Zhi, C. Nanoporous $CaCO_3$ Coatings Enabled Uniform Zn Stripping/Plating for Long-Life Zinc Rechargeable Aqueous Batteries. *Adv. Energy Mater.* **2018**, *8* (25), No. 1801090.

(15) Wang, S.-B.; Ran, Q.; Yao, R.-Q.; Shi, H.; Wen, Z.; Zhao, M.; Lang, X.-Y.; Jiang, Q. Lamella-nanostructured eutectic zinc−aluminum alloys as reversible and dendrite-free anodes for aqueous rechargeable batteries. *Nat. Commun.* **2020**, *11* (1), 1634.

(16) Cao, L.; Li, D.; Hu, E.; Xu, J.; Deng, T.; Ma, L.; Wang, Y.; Yang, X.-Q.; Wang, C. Solvation Structure Design for Aqueous Zn Metal Batteries. *J. Am. Chem. Soc.* **2020**, *142* (51), 21404−21409.

(17) Bayaguud, A.; Luo, X.; Fu, Y.; Zhu, C. Cationic Surfactant-Type Electrolyte Additive Enables Three-Dimensional Dendrite-Free Zinc Anode for Stable Zinc-Ion Batteries. *ACS Energy Lett.* **2020**, *5* (9), 3012−3020.

(18) Huang, C.; Zhao, X.; Liu, S.; Hao, Y.; Tang, Q.; Hu, A.; Liu, Z.; Chen, X. Stabilizing Zinc Anodes by Regulating the Electrical Double Layer with Saccharin Anions. *Adv. Mater.* **2021**, *33* (38), No. 2100445.

(19) Zhao, R.; Wang, H.; Du, H.; Yang, Y.; Gao, Z.; Qie, L.; Huang, Y. Lanthanum nitrate as aqueous electrolyte additive for favourable zinc metal electrodeposition. *Nat. Commun.* **2022**, *13* (1), 3252.

(20) Groß, A.; Sakong, S. Modelling the electric double layer at electrode/electrolyte interfaces. *Curr. Opin. Electrochem.* **2019**, *14*, 1−6.

(21) Huang, J.; Li, Z.; Ge, H.; Zhang, J. Analytical Solution to the Impedance of Electrode/Electrolyte Interface in Lithium-Ion Batteries. *J. Electrochem. Soc.* **2015**, *162* (13), A7037−A7048.
(22) Yan, C.; Li, H.-R.; Chen, X.; Zhang, X.-Q.; Cheng, X.-B.; Xu, R.; Huang, J.-Q.; Zhang, Q. Regulating the Inner Helmholtz Plane for Stable Solid Electrolyte Interphase on Lithium Metal Anodes. *J. Am. Chem. Soc.* **2019**, *141* (23), 9422−9429.
(23) Borodin, O.; Ren, X.; Vatamanu, J.; von Wald Cresce, A.; Knap, J.; Xu, K. Modeling Insight into Battery Electrolyte Electrochemical Stability and Interfacial Structure. *Acc. Chem. Res.* **2017**, *50* (12), 2886−2894.
(24) Morin-Crini, N.; Fourmentin, S.; Fenyvesi, É.; Lichtfouse, E.; Torri, G.; Fourmentin, M.; Crini, G. 130 years of cyclodextrin discovery for health, food, agriculture, and the industry: a review. *Environ. Chem. Lett.* **2021**, *19* (3), 2581−2617.
(25) Crini, G. Review: A History of Cyclodextrins. *Chem. Rev.* **2014**, *114* (21), 10940−10975.
(26) Zhao, K.; Fan, G.; Liu, J.; Liu, F.; Li, J.; Zhou, X.; Ni, Y.; Yu, M.; Zhang, Y.-M.; Su, H.; Liu, Q.; Cheng, F. Boosting the Kinetics and Stability of Zn Anodes in Aqueous Electrolytes with Supramolecular Cyclodextrin Additives. *J. Am. Chem. Soc.* **2022**, *144* (25), 11129−11137.
(27) Qiu, M.; Sun, P.; Wang, Y.; Ma, L.; Zhi, C.; Mai, W. Anion-Trap Engineering toward Remarkable Crystallographic Reorientation and Efficient Cation Migration of Zn Ion Batteries. *Angew. Chem., Int. Ed.* **2022**, *61* (44), e202210979.
(28) Qu, Q.; Tucker, E.; Christian, S. D. Sulfoalkyl ether beta-cyclodextrin derivatives: Synthesis and characterizations. *J. Incl. Phenom. Macrocycl. Chem.* **2002**, *43* (3−4), 213−221.
(29) Luna, E. A.; Bornancini, E. R. N.; Tait, R. J.; Thompson, D. O.; Stobaugh, J. F.; Rajewski, R. A.; Stella, V. J. Evaluation of the utility of capillary electrophoresis for the analysis of sulfobutyl ether beta-cyclodextrin mixtures. *J. Pharm. Biomed. Anal.* **1996**, *15* (1), 63−71.
(30) Bian, H.; Wen, X.; Li, J.; Chen, H.; Han, S.; Sun, X.; Song, J.; Zhuang, W.; Zheng, J. Ion clustering in aqueous solutions probed with vibrational energy transfer. *Proc. Natl. Acad. Sci. U.S.A.* **2011**, *108* (12), 4737−4742.
(31) Sakamoto, S.; Kawase, Y. Adsorption capacities of poly-γ-glutamic acid and its sodium salt for cesium removal from radioactive wastewaters. *J. Environ. Radioact.* **2016**, *165*, 151−158.
(32) Dai, H.; Gu, X.; Dong, J.; Wang, C.; Lai, C.; Sun, S. Stabilizing lithium metal anode by octaphenyl polyoxyethylene-lithium complexation. *Nat. Commun.* **2020**, *11* (1), 643.
(33) Favaro, M.; Jeong, B.; Ross, P. N.; Yano, J.; Hussain, Z.; Liu, Z.; Crumlin, E. J. Unravelling the electrochemical double layer by direct probing of the solid/liquid interface. *Nat. Commun.* **2016**, *7* (1), 12695.
(34) Mizuno, Y.; Okubo, M.; Asakura, D.; Saito, T.; Hosono, E.; Saito, Y.; Oh-ishi, K.; Kudo, T.; Zhou, H. Impedance spectroscopic study on interfacial ion transfers in cyanide-bridged coordination polymer electrode with organic electrolyte. *Electrochim. Acta* **2012**, *63*, 139−145.
(35) Walsh, F. C.; Herron, M. E. Electrocrystallization and electrochemical control of crystal-growth-fundamental considerations and electrodeposition of materials. *J. Phys. D-Appl. Phys.* **1991**, *24* (2), 217−225.
(36) Hu, J.; Ren, W.; Chen, X.; Li, Y.; Huang, W.; Yang, K.; Yang, L.; Lin, Y.; Zheng, J.; Pan, F. The role of anions on the Helmholtz Plane for the solid-liquid interface in aqueous rechargeable lithium batteries. *Nano Energy* **2020**, *74*, No. 104864.
(37) Zhang, Q.; Hua, Y. Effects of 1-butyl-3-methylimidazolium hydrogen sulfate-[BMIM]HSO_4 on zinc electrodeposition from acidic sulfate electrolyte. *J. Appl. Electrochem.* **2009**, *39* (2), 261−267.
(38) Pei, A.; Zheng, G.; Shi, F.; Li, Y.; Cui, Y. Nanoscale Nucleation and Growth of Electrodeposited Lithium Metal. *Nano Lett.* **2017**, *17* (2), 1132−1139.
(39) Extrand, C. W. A thermodynamic model for wetting free energies from contact angles. *Langmuir* **2003**, *19* (3), 646−649.
(40) Zhi, J.; Li, S.; Han, M.; Chen, P. Biomolecule-guided cation regulation for dendrite-free metal anodes. *Sci. Adv.* **2020**, *6* (32), No. eabb1342.
(41) Yang, H.; Chang, Z.; Qiao, Y.; Deng, H.; Mu, X.; He, P.; Zhou, H. Constructing a Super-Saturated Electrolyte Front Surface for Stable Rechargeable Aqueous Zinc Batteries. *Angew. Chem., Int. Ed.* **2020**, *59* (24), 9377−9381.
(42) Zhao, Z.; Zhao, J.; Hu, Z.; Li, J.; Li, J.; Zhang, Y.; Wang, C.; Cui, G. Long-life and deeply rechargeable aqueous Zn anodes enabled by a multifunctional brightener-inspired interphase. *Energy Environ. Sci.* **2019**, *12* (6), 1938−1949.
(43) Ma, L.; Li, Q.; Ying, Y.; Ma, F.; Chen, S.; Li, Y.; Huang, H.; Zhi, C. Toward Practical High-Areal-Capacity Aqueous Zinc-Metal Batteries: Quantifying Hydrogen Evolution and a Solid-Ion Conductor for Stable Zinc Anodes. *Adv. Mater.* **2021**, *33* (12), No. 202007406.
(44) Hao, J.; Li, B.; Li, X.; Zeng, X.; Zhang, S.; Yang, F.; Liu, S.; Li, D.; Wu, C.; Guo, Z. An In-Depth Study of Zn Metal Surface Chemistry for Advanced Aqueous Zn-Ion Batteries. *Adv. Mater.* **2020**, *32* (34), No. 2003021.
(45) Zhang, Q.; Luan, J.; Huang, X.; Wang, Q.; Sun, D.; Tang, Y.; Ji, X.; Wang, H. Revealing the role of crystal orientation of protective layers for stable zinc anode. *Nat. Commun.* **2020**, *11* (1), 3961.
(46) Deng, C.; Xie, X.; Han, J.; Tang, Y.; Gao, J.; Liu, C.; Shi, X.; Zhou, J.; Liang, S. A Sieve-Functional and Uniform-Porous Kaolin Layer toward Stable Zinc Metal Anode. *Adv. Funct. Mater.* **2020**, *30* (21), No. 2000599.
(47) Zeng, X.; Xie, K.; Liu, S.; Zhang, S.; Hao, J.; Liu, J.; Pang, W. K.; Liu, J.; Rao, P.; Wang, Q.; Mao, J.; Guo, Z. Bio-inspired design of an in situ multifunctional polymeric solid−electrolyte interphase for Zn metal anode cycling at 30 mA cm^{-2} and 30 mA h cm^{-2}. *Energy Environ. Sci.* **2021**, *14* (11), 5947−5957.
(48) Li, Y.; Wu, P.; Zhong, W.; Xie, C.; Xie, Y.; Zhang, Q.; Sun, D.; Tang, Y.; Wang, H. A progressive nucleation mechanism enables stable zinc stripping−plating behavior. *Energy Environ. Sci.* **2021**, *14* (10), 5563−5571.
(49) Sun, P.; Ma, L.; Zhou, W.; Qiu, M.; Wang, Z.; Chao, D.; Mai, W. Simultaneous Regulation on Solvation Shell and Electrode Interface for Dendrite-Free Zn Ion Batteries Achieved by a Low-Cost Glucose Additive. *Angew. Chem., Int. Ed.* **2021**, *60* (33), 18247−18255.
(50) Qin, R.; Wang, Y.; Zhang, M.; Wang, Y.; Ding, S.; Song, A.; Yi, H.; Yang, L.; Song, Y.; Cui, Y.; Liu, J.; Wang, Z.; Li, S.; Zhao, Q.; Pan, F. Tuning Zn^{2+} coordination environment to suppress dendrite formation for high-performance Zn-ion batteries. *Nano Energy* **2021**, *80*, No. 105478.
(51) Chu, Y.; Zhang, S.; Wu, S.; Hu, Z.; Cui, G.; Luo, J. In situ built interphase with high interface energy and fast kinetics for high performance Zn metal anodes. *Energy Environ. Sci.* **2021**, *14* (6), 3609−3620.
(52) Li, D.; Cao, L.; Deng, T.; Liu, S.; Wang, C. Design of a Solid Electrolyte Interphase for Aqueous Zn Batteries. *Angew. Chem., Int. Ed.* **2021**, *60* (23), 13035−13041.
(53) Zeng, X.; Mao, J.; Hao, J.; Liu, J.; Liu, S.; Wang, Z.; Wang, Y.; Zhang, S.; Zheng, T.; Liu, J.; Rao, P.; Guo, Z. Electrolyte Design for In Situ Construction of Highly Zn^{2+}-Conductive Solid Electrolyte Interphase to Enable High-Performance Aqueous Zn-Ion Batteries under Practical Conditions. *Adv. Mater.* **2021**, *33* (11), No. 2007416.
(54) Pan, H.; Shao, Y.; Yan, P.; Cheng, Y.; Han, K. S.; Nie, Z.; Wang, C.; Yang, J.; Li, X.; Bhattacharya, P.; Mueller, K. T.; Liu, J. Reversible aqueous zinc/manganese oxide energy storage from conversion reactions. *Nat. Energy* **2016**, *1* (5), 16039.
(55) Gao, X.; Wu, H.; Li, W.; Tian, Y.; Zhang, Y.; Wu, H.; Yang, L.; Zou, G.; Hou, H.; Ji, X. H^+-Insertion Boosted α-MnO_2 for an Aqueous Zn-Ion Battery. *Small* **2020**, *16* (5), No. 1905842.
(56) Hutter, J.; Iannuzzi, M.; Schiffmann, F.; VandeVondele, J. CP2K: atomistic simulations of condensed matter systems. *Wiley Interdiscip. Rev.-Comput. Mol. Sci.* **2014**, *4* (1), 15−25.

https://doi.org/10.1021/acsnano.3c03220
ACS Nano 2023, 17, 24619−24631

(57) Perdew, J. P.; Burke, K.; Ernzerhof, M. Generalized gradient approximation made simple. *Phys. Rev. Lett.* **1996**, *77* (18), 3865−3868.
(58) Grimme, S. Semiempirical GGA-type density functional constructed with a long-range dispersion correction. *J. Comput. Chem.* **2006**, *27* (15), 1787−1799.
(59) VandeVondele, J.; Hutter, J. Gaussian basis sets for accurate calculations on molecular systems in gas and condensed phases. *J. Chem. Phys.* **2007**, *127* (11), 114105.
(60) VandeVondele, J.; Krack, M.; Mohamed, F.; Parrinello, M.; Chassaing, T.; Hutter, J. Quickstep: Fast and accurate density functional calculations using a mixed Gaussian and plane waves approach. *Comput. Phys. Commun.* **2005**, *167* (2), 103−128.
(61) Goedecker, S.; Teter, M.; Hutter, J. Separable dual-space Gaussian pseudopotentials. *Phys. Rev. B* **1996**, *54* (3), 1703−1710.
(62) Hartwigsen, C.; Goedecker, S.; Hutter, J. Relativistic separable dual-space Gaussian pseudopotentials from H to Rn. *Phys. Rev. B* **1998**, *58* (7), 3641−3662.

https://doi.org/10.1021/acsnano.3c03220
ACS Nano 2023, 17, 24619−24631